Journal of Electron Spectroscopy and Related Phenomena 267 (2023) 147381

Contents lists available at ScienceDirect

Journal of Electron Spectroscopy and Related Phenomena

journal homepage: www.elsevier.com/locate/elspec

Scanning transmission X-ray microscopy at the Advanced Light Source

Thomas Feggeler [a,b,*], Abraham Levitan [c,b], Matthew A. Marcus [b], Hendrik Ohldag [b,d,e], David A. Shapiro [b]

[a] Department of Physics, University of California, Berkeley, Berkeley, CA 94720, United States
[b] Advanced Light Source, Lawrence Berkeley National Laboratory, Berkeley, CA 94720, United States
[c] Massachusetts Institute of Technology, Cambridge, MA 02139, United States
[d] Department of Material Sciences and Engineering, Stanford University, Stanford, CA 94305, United States
[e] Department of Physics, University of California, Santa Cruz, Santa Cruz, CA 95064, United States

ARTICLE INFO

Keywords:
X-rays
Microscopy
Ptychography
Tomography
STXM
Time-resolved
Magnetic resonance

ABSTRACT

Over 50 years of development, synchrotron based X-ray microscopy has become a routine and powerful tool for the analysis of nanoscale structure and chemistry in many areas of science. Scanning X-ray microscopy is particularly well suited to the study of chemical and magnetic states of matter and has become available at most synchrotron light sources using a variety of optical schemes, detectors and sample environments. The Advanced Light Source at Lawrence Berkeley National Laboratory has an extensive program of soft X-ray scanning microscopy which supports a broad range of scientific research using a suite of advanced tools for high spatio-temporal resolution and control of active materials. Instruments operating within an energy range between 200–2500 eV with spatial resolution down to 7 nm and sub 20 picosecond time resolution are available. These capabilities can be routinely used in combination with a variety of sample stimuli, including gas or fluid flow, temperature control from 100 to 1200 K, DC bias and pulsed or continuous microwave excitation. We present here a complete survey of our instruments, their most advanced capabilities and a perspective on how they complement each other to solve complex problems in energy, materials and environmental science.

1. Introduction

The development of X-ray microscopy began with point projection microscopy in the few decades following the discovery of X-rays in 1895 by Wilhelm Conrad Röntgen. It was not until the early 1970's that elemental analysis with a focused micro-beam became possible using parasitic synchrotron radiation from an electron accelerator. Like point projection microscopes, the spatial resolution was limited to several microns by the use of grazing incidence reflective optics for focusing. The fabrication of Fresnel zone plate lenses, first by holographic methods and later by electron beam lithography, finally led to spatial resolutions below 100 nanometers. By the mid-1980's, development of X-ray nanoprobe instruments was rapid with efforts at Daresbury in the UK, BESSY in Germany and the NSLS in the US. The first high brightness insertion device was used for scanning X-ray microscopy and new high brightness synchrotrons were being built which would be ideal sources for this new scientific tool. An excellent overview is given in the reviews [1,2].

In the early 1990's, the Advanced Light Source was well positioned to be a world leader in the development of scanning X-ray microscopy as it was the first third generation synchrotron source (i.e. designed specifically to accommodate high brightness insertion devices) and due to its close relationship with the Center for X-ray Optics at Lawrence Berkeley National Laboratory [3]. Indeed, between 1995 and 2010 the number of scanning microscopes available to the ALS community expanded from one instrument on an insertion device beamline to three instruments, one insertion device beamline and two bending magnet beamlines [4,5]. This collection of instruments covered a broad energy range, from about 200 eV to over 2000 eV, providing chemical sensitivity to all elements heavier than boron and provided about 12500 operating hours annually to the scientific community.

Since 2010, the ALS Microscopy Program has evolved further to provide more access to more specialized and capable instruments with modernized scanning systems, controls, detectors and data acquisition. Currently four microscopes are operational, two on insertion devices and two on a bending magnet source, providing an even broader energy range of 200–2500 eV and access to advanced methods like ptychography, tomography, time-resolved photon counting, *operando* environments for electrochemistry, catalysis and cryogenic samples [6,7]. The sections below give an overview of the available instruments, their advanced functionality as it relates to energy materials in particular and a short review of representative scientific results.

* Corresponding author at: Department of Physics, University of California, Berkeley, Berkeley, CA 94720, United States.
E-mail address: tfeggeler@berkeley.edu (T. Feggeler).

https://doi.org/10.1016/j.elspec.2023.147381
Received 30 May 2023; Received in revised form 17 July 2023; Accepted 18 July 2023
Available online 22 July 2023

2. Scanning soft X-ray microscopes available at the ALS

The imaging beamlines and microscopes at the ALS largely fall into two categories. The insertion device beamlines utilize an entrance slitless design with collimated plane grating monochromators and torroidal refocusing mirrors. This design is common among imaging beamlines at other facilities because it can provide high flux but also flexibility in balancing the tradeoff between high flux and high energy resolution while the monochromator itself can provide good isolation from harmonic light. Meanwhile the bending magnet beamlines utilize an optical scheme which minimizes reflections for high efficiency. A toroidal mirror focuses on both entrance and exit slit while a spherical grating monochromator provides good energy resolution over a usefully broad X-ray spectrum. (Fig. 1) gives an overview on the experimental parameters of the available instruments.

2.1. Beamline 5.3.2

The bending-magnet beamlines are described in [8] . The 5.3.2 port splits into two similar beamlines optimized for differing energy ranges. The lower-energy port 5.3.2.2 has a spherical-grating monochromator with a single grating, which images an entrance slit onto a set of exit slits which serve as the source for a zone-plate STXM typically operating with a zone plate having a 30 nm outer width. The optics are coated with Ni to help suppress harmonics. In addition, a 1m-long differential-pumped section can be filled with nitrogen in order to suppress second-harmonic light when running at the C edge. The energy resolution is optimized for the CNO K-edges, but the beamline provides flux up to 800 eV, so transition metals up to Co can be studied at L-edges. Typical uses of 5.3.2.2 include the study of atmospheric aerosols, organic photovoltaic materials (see below), Li-Fe battery materials and organics in meteorites and asteroids. Beamline 5.3.2.1 features a monochromator with two gratings so as to be able to run over an extended energy range, from about 400 eV to 2000 eV . Both microscopes can be set up to perform operando measurements and take samples on TEM grids or SiN windows. Both beamlines can be run in vacuum or up to 200 Torr of gas, usually He.

2.2. Beamline 7.0.1.2

The insertion device beamlines in ALS straight section 7.0.1 are described in [9] and the scanning microscope on branchline 7.0.1.2 is described in detail here [6,10]. Briefly, the beamline source is an elliptically polarizing undulator with 38 mm period and minimum gap of 10.5 mm which provides full polarization control, left/right circular and continuously variable linear polarization from horizontal to vertical, across an energy range of 250 eV to 2500 eV. This provides chemical sensitivity to the K absorption edge for elements carbon to sulfur, the L edge for chlorine through molybdenum and the M edge for technetium through lead. The *N* edges of heavier elements, like the actinides are also accessible. The monochromator is a collimated plane grating which provides a moderate energy resolving power ($E/\Delta E$) of 2500 and allows for a flexible trade-off between resolution, range, efficiency and harmonic suppression. Optics are Rhodium coated for an extended energy range and a torroidal mirror focuses onto the coherence defining exit slit which illuminates the nanofocusing zone plate optic three meters downstream.

The Nanosurveyor endstation operates as a conventional scanning microscope with 45 nm zone plate focus and silicon diode detector for total transmission measurements but it has a few key characteristics which make it unique. First, the vacuum chamber can accept commercial sample holders developed for transmission electron microscopes. This use of standardized sample equipment makes the introduction of a variety of sample environments, e.g. fluid or gas flow, trivial, though their effective use on particular material systems may remain challenging. Second, a high frame rate charge coupled device detector (CCD) is used for coherent scattering measurements which can be used for a variety of computational imaging methods like ptychography or randomized probe imaging. These methods can achieve a spatial resolution limited by the dose delivered to the sample which has reached as low as 7 nm full period. Because of the high X-ray doses required for high spatial resolution imaging, typical uses are the study of hard materials like characterization of the oxidation or spin states in transition metal based energy storage or conversion materials or magnetic thin films.

2.3. Beamline 11.0.2.2

Beamline 11.0.2.2 is an elliptical undulator beamline that allows for full polarization control between 200 eV and 2000 eV [11]. The beamline is designed for energies as low as 100 eV but due to the very short focal length of our high resolution zoneplates, typical STXM operation is restricted to energies above 200 eV. The beamline consists of a cylindrical horizontally collimating mirror, a plane grating monochromator and a toroidal re-focussing mirror that directs the beam onto a two dimensional exit slit aperture. The typical resolving power of the monochromator is between 3000–5000. The vertical slit is used to select the photon energy, while the horizontal slits are electrically isolated and the differential electron yield of the slits is used to control the horizontal deflection angle of the toroidal mirror in a feedback loop. The microscope is located approximately 2.5 m downstream of the aperture.

Experimenters have the choice of using zoneplates with 18 nm, 25 nm or 45 nm outer zone width. The diameter of the zone plate varies between 240 μm and 360 μm. The setups offers different detection methods. Standard detection of transmission yield is achieved via commercial X-ray photodiodes (e.g. AXUV100). Implementation of electron and fluorescence yield detection is currently under way. In addition high speed avalanche photodiodes with rise times faster than 1 ns are used to register individual synchrotron X-ray pulses for time resolved measurements.

Typical spectromicroscopy operation involves mounting of up to eight samples simultaneously on standardized metal plates. This sample mount also accommodates in-situ gas and liquid cells provided by Norcada [12]. The sample mount can be changed within minutes to also accommodate in-situ liquid and gas flow cells manufactured by Hummingbird. Finally, to address challenges in solid state physics, the sample environment is extended with the capability to apply magnetic fields up to 0.5 Tesla parallel or perpendicular to the X-ray beam. In addition the option to control the sample temperature between 25 K and 500 K will be added in the near future.

3. Advanced capabilities

Scanning X-ray microscopy has developed into a routine tool which is available at every synchrotron in either the soft or hard X-ray variety. In this section, we highlight some advanced tools which have become routinely available at the ALS but which may be in earlier stages of development elsewhere.

3.1. Instrument controls

We have developed a pure Python based control system for STXM, called pystxmcontrol, which has been deployed for general use at beamline 7.0.1.2 and is currently being ported to the other beamlines (Fig. 2). The software uses a client–server approach where the server runs on a computer with direct access to the microscope hardware and the client can run on any computer with network access to the server for communication of commands and receipt of data for visualization. A primary objective in the design philosophy was to minimize software overhead by utilizing advanced controller functionality for piezo scanning and STXM data acquisition. Python interfaces with minimal

ALS ADVANCED LIGHT SOURCE	Beamline 5.3.2.1 Scanning Transmission X-ray Microscopy	Beamline 5.3.2.2 Polymer Scanning Transmission X-ray Microscopy	Beamline 7.0.1.2 Coherent Scattering and Microscopy (COSMIC) - Imaging	Beamline 11.0.2.2 Molecular Environmental Science Scanning Transmission X-ray Microscopy
Energy Range (eV)	500 - 2000	200 - 800	250 - 2500	200 - 2000
Accessible Elements (atomic Number)	8 - 14 (K) 22 - 36 (L) 51 - 75 (M)	6 - 9 (K) 17 - 27 (L) 41 - 56 (M)	6 - 16 (K) 17 - 41 (L) 43 - 82 (M)	6 - 14 (K) 17 - 37 (L) 41 - 75 (M)
Peak Flux on Sample (at eV)	10^6 at 500	10^6 at 300	10^9 at 500	$5 \cdot 10^8$ at 500
Detection	PMT	PMT	PIN diode / fast CCD	PIN / APD
Polarization	Linear horizontal	Linear horizontal	Inclined linear, circular	Inclined linear, circular
Spatial Resolution (nm)	30	30	50 (7)	30, 50
Time Resolution (Pixel Dwell Time) (ms)	1 - 5	1 - 5	0.1 (100)	1 (< 20 ps)
Sample Environment	0.2 bar He, gas, liquid	0.2 bar He, gas, liquid	Vacuum, gas, liquid, cryo, ambient	0.2 bar He, gas, liquid, ambient
Sample Stimulus	Bias, heat	Bias, heat	Bias, heat	Bias, heat, microwave, magnetic field
Scientific Focus	Soft materials	Soft materials	Hard materials	Devices, magnetic materials

Fig. 1. Capability matrix of the microscopy program beamlines at the Advanced Light Source.

communication were developed for the nPoint LC400 piezo controller and Keysight 52320 A counter, though the use of abstract classes for each interface means that others can be readily implemented without changing higher level code. Access to hardware using the EPICS, or any other control system, is also readily implemented using the same abstract classes and a simple JSON text file is used to fully configure the motor system and build relevant components in the graphical interface. The software overhead for a typical STXM scan of 100 × 100 pixels is about 65 microseconds per pixel which is about 7% of the typical per pixel dwell time. Though the software overhead is actually accumulated on a per trajectory basis rather than per pixel so larger scans can achieve overheads of below 1%.

Pystxmcontrol also provides a ZeroMQ (ZMQ) based interface to imaging detectors and downstream analysis pipelines. The graphical interface can subscribe to a ZMQ data stream for open loop visualization while the server will subscribe in a closed loop fashion, ensuring that each frame is received. The server will also publish the frame with scan relevant metadata so that downstream analysis pipelines can work on the data during the scan. If those pipelines also publish the calculation results, the graphical interface can subscribe for real-time visualization of the computed images. Fig. 2 shows the layout of the graphical interface with scan definition and motor controls on the left and a live display of a randomized probe imaging reconstruction. Randomized probe imaging is described in section 3.6.

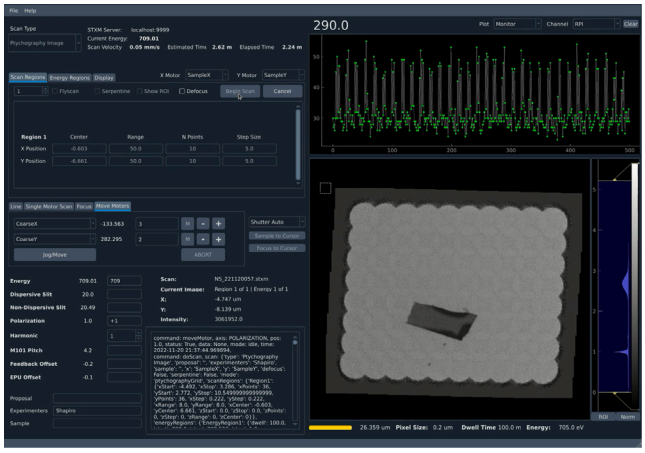

Fig. 2. Graphical user interface at beamline 7.0.1.2. Scans are graphically defined by the user and the data are immediately displayed during acquisition. Shown here is the result of a real time reconstruction of a large field of view using randomized probe imaging. Data are automatically sent to a remote GPU array for processing and the result is returned to the graphical interface for visualization during the scan.

3.2. Ptychographic spectromicroscopy

Since STXM inherently requires a localized, intense and coherent X-ray illumination, it is an ideal platform for the implementation of coherent scattering based computational imaging methods like ptychography which compute high resolution images from a set of localized coherent scattering patterns. The only instrument modification required is the use of a detector with many pixels rather than a single pixel [13,14]. Most implementations of ptychography require up to a megapixel or more in each of many thousands of diffraction patterns which comprise a single image scan, thus, the data volume is extraordinary. The primary technical challenges are the high frame rate soft X-ray detector with single photon sensitivity, which is not commercially available, the transparent implementation of high performance reconstruction algorithms, which require integrated high performance computing, and the development of such algorithms.

Ptychography is broadly developed by the X-ray microscopy community and is available in some form at most synchrotrons. The effort at the ALS has focused on developing a user friendly ptychography instrument with world leading spatial resolution applied to two dimensional spectromicroscopy of hard materials. This arises naturally from the strength and weakness of using soft X-rays, namely the chemical sensitivity and short penetration depth respectively. As an example, the penetration depth of a crystalline material containing a large fraction of a transition metal will be only a few hundred nanometers at the relevant absorption edges. Regardless, the ability to measure heterogeneity well below such length scales is extremely powerful for many areas of science, particularly the study chemical phase changes

in energy storage and conversion materials. Using ptychography for two-dimensional chemical composition mapping, we have shown that it removes spectral distortions that are inherent to conventional microscopy [15] and that the phase information it naturally provides can be used for improve chemical sensitivity. These benefits are in addition to the improved spatial resolution which is nearly a factor of 10 better than conventional microscopy.

3.3. Operando spectromicroscopy

A STXM instrument allows the user to obtain information about the electronic structure of an atomic species in a sample of interest. Soft X-ray absorption is used as a contrast mechanism, which is able to provide information about the distribution and symmetry of unoccupied valence states at the Fermi energy of the material. These states can be used to distinguish different chemical species of a particular atom [16]. The traditional approach is to prepare a sample of interest in a certain state and then mount it in a STXM to study the chemical state. However, this approach can only provide delayed information about the state of a sample and relies on the assumption that the sample does not change between preparation and data acquisition. This limitation has driven the development of *in operando* spectromicroscopy over the past decade. The particular advantage of acquiring soft X-ray spectromicroscopy in transmission is that it is a so called *photon in - photon out* technique. Since neither the incoming or the outgoing photon is affected by changes to the local environment (electric potential, magnetic fields etc.) it allows us to study materials at work or *in operando*. One significant limitation is the limited penetration depth of soft X-rays, so that the sample has to be contained in a rather thin layer of ambient atmosphere or liquid, typically a few hundred nanometers thick. Another limitation is that the focal plane is, for soft X-rays, close to the OSA, so an in-situ cell must have a very limited thickness between the sample and the upstream surface of the cell. Suitable micromachined cells have been developed for electron microscopy and adapted for STXM, and other geometries have been developed, e.g. the one described in [17].

3.4. Time resolved spectromicroscopy

Time-resolved magnetic X-ray spectromicroscopy uses the X-ray Circular Magnetic Dichroism (XMCD) effect to probe the dynamic response of the magnetization of specific elements within a magnetic material exhibiting (field-induced) magnetic order. XMCD reveals orientation and magnitude of magnetic moments by recording X-ray absorption data with circularly polarized X-rays with different helicity. The typical geometries used for time-resolved XMCD measurements are the averaging detection in the so-called longitudinal XMCD geometry. Here the length difference ΔM_z between the length of the magnetization vector $M_{Equilibrium}$ and the projection of the precessing magnetization M on $M_{Equilibrium}$ is measured with the k-vector of the probing X-rays being parallel to $M_{Equilibrium}$ and an applied external magnetic field B_{Ext}. A true time- and phase -resolved detection is realized in the so-called transverse geometry, probing the oscillating $\Delta M^{\perp}$ component of M in the sub 20 picosecond regime in standard multi bunch mode using an avalanche photo diode.

Both geometries have been employed in the spectroscopic technique of X-ray detected Ferromagnetic Resonance (XFMR) [18–24]. The transverse geometry is typically used in combination with the spatially resolved technique of Time-Resolved Scanning Transmission X-ray Microscopy (TR-STXM) and its variety STXM detected Ferromagnetic Resonance (STXM-FMR) combining a spatial resolution better than 50 nm with picosecond time sampling [25–29]. A stroboscopic detection scheme is realized by phase-locking the employed periodic excitation, e.g. a microwave b_{hf}, to the synchrotron frequency f_s (500 MHz at the ALS). Hereby the frequency of the excitation corresponds to a higher harmonic of f_s. The setup realized at ALS beamline 11.0.2.2 is

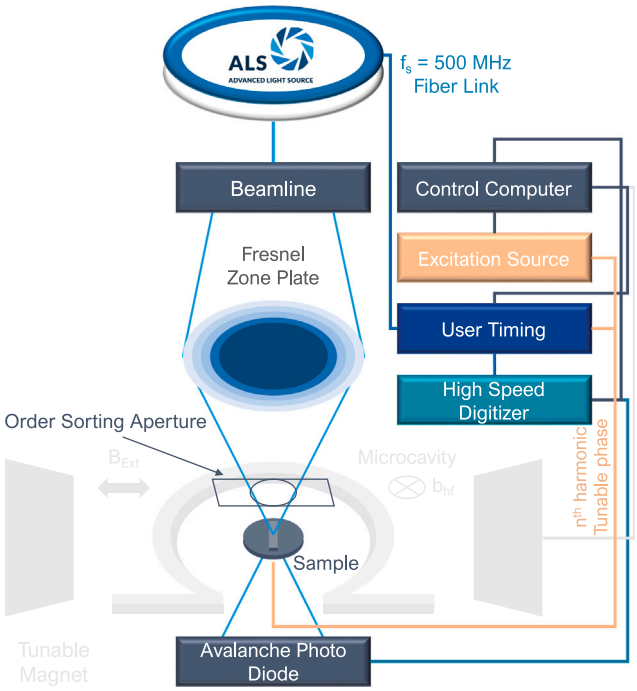

Fig. 3. Schematic representation of the TR-STXM setup realized at ALS beamline 11.0.2.2. The STXM is situated in a high-vacuum chamber. Gray colored parts are optional components for (dynamic) magnetic measurements.

shown in figure 3 depicting a configuration for magnetic measurements using a microcavities/resonator [30] for a defined magnetic resonance geometry in transverse orientation. An optional static magnetic bias field B_{Ext} is generated by a set of oppositely facing Nd permanent magnets with their distance being varied for different field strength.

The STXM is operated under high-vacuum conditions with pressures at $\sim 10^{-6}$ Torr, using Fresnel zone plates down to 18 nm outer zone width for focusing the X-ray beam onto the sample. This scans a sample pixel by pixel for a certain integration time with the detection realized by an Si avalanche photo diode of the Hamamatsu S12426 series with a diameter of 0.5 mm is employed for the time-resolved measurements. The phase-lock of the tunable sample excitation frequency to f_s is realized using the ALS developed User Timing System, delivering a synchronized timing event stream to the ALS developed High Speed Digitizer for experimental dynamic sampling. By tuning the excitation phase a set of phases of the dynamic response of the sample is detected. By using a detection scheme recording TR-STXM image sets with and without external dynamic stimuli, the excitation induced X-ray transmission is extracted. Successively, the spatial amplitude and phase map of the magnetization can be obtained by using a pixel-by-pixel sinusoidal fitting procedure on the recorded times series of images, color coding the phase relative to$t$ = 0 ps as the hue, the amplitude as brightness [31–33] and the fit accuracy as color saturation [31]. By using the same phase and amplitude analysis on complementary micromagnetic simulation data, it is possible to correlate the experimental and simulated dynamic response of a sample.

3.5. Coherent full-field microscopy

The various X-ray microscopy experiments described above are all scanning methods, which operate by scanning a focused beam of X-rays over a sample. However, there are certain advantages to full-field microscopy that make it a valuable complement to scanning methods. Specifically, full-field microscopy has a natural advantage for time-resolved studies and parametric sweeps, because the acquisition speed

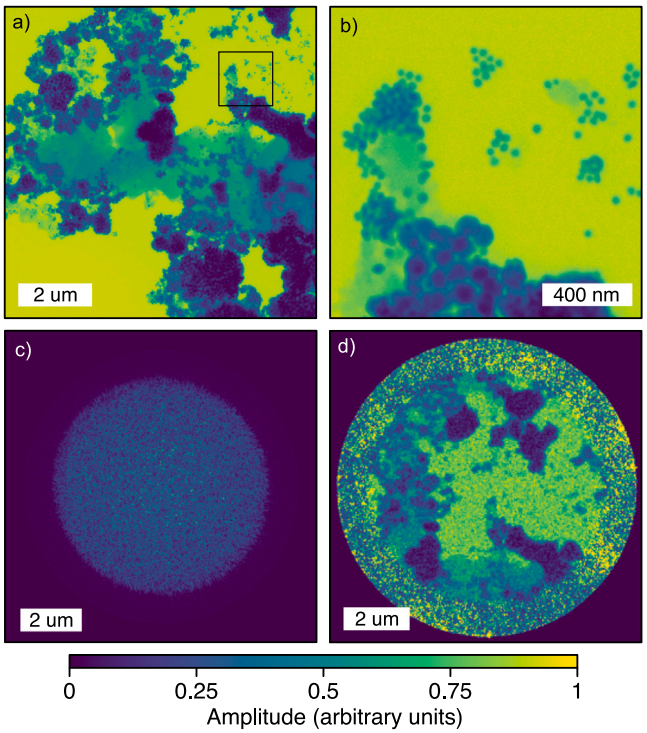

Fig. 4. (a) Section of a ptychography reconstruction of 40 nm and 100 nm gold nanoparticles on a silicon nitride membrane, using 3000 diffraction frames. (b) Zoomed region of the same reconstruction, which achieves a full-pitch resolution of 21 nm, estimated via the Fourier ring correlation. (c) The focal spot of the RPI compatible optic used for this reconstruction. (d) A full-field image of the same sample, analyzed using RPI.
Source: Adapted from Ref. [35]

is limited by flux and frame rate, rather than the speed of mechanical motion.

Recognizing the value of having a fast full-field microscope available, a microscopy method called Randomized Probe Imaging (RPI) [34] has been implemented at beamline 7.0.1.2 to complement the scanning ptychography microscope. The implementation consists of a custom zone plate optic, which projects a 6.75 μm diameter circular spot onto the sample. This illumination has a speckled texture on a length scale of 30 nm, enabling full-field images to be captured with resolutions in principle down to 60 nm after analysis with software also available at the beamline.

The unusual aspect of this setup is its compatibility with both ptychography and full-field imaging. Because the illumination spot is highly coherent, it is still possible to collect ptychography data using the RPI-compatible optics, and the data can be remarkably high quality as seen in Fig. 4. However, it is also possible to collect full-field images. The time savings associated with full-field imaging promise to dramatically speed up spectroscopic and tomographic data collection, while also opening up direct access to millisecond-scale dynamics.

4. Recent applications

The ALS Microscopy Program provides a holistic toolbox for spatially-resolved X-ray characterization in materials science, physics, chemistry, biology and medicine. Recent examples of facility use show the manifold fields of interest of the users of the microscopy program beamlines.

4.1. Organic photovoltaic material development

Organic photovoltaic (OPV) materials consist of blends of two or more organic semiconductors which are segregated into donor-rich and

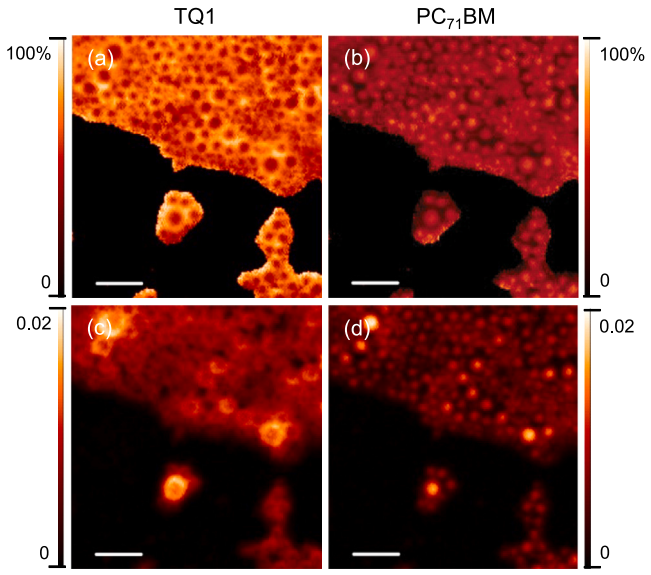

Fig. 5. Composition mapping of a core–shell material similar to that described in [43]. The scalebars are 500 nm. (a) mass fraction of TQ1 component; (b) mass fraction of PC71BM component, (c,d) corresponding column densities in mg/cm2.

acceptor-rich domains. The interfaces between these domains form p–n junctions which facilitate the splitting of excitons into their component carriers. Thus, when light is absorbed, electrons are drawn to the acceptor regions, and eventually to one electrode and holes to the donor regions and then to the other electrode [36]. Due to the low dielectric constant of the organic semiconductors, the exciton radius is only of order 10 nm, so the morphology must be of that scale for the devices to work. One therefore needs methods to probe the morphology of organic materials at that scale, with chemical sensitivity since the components tend to have similar densities and include the same elements. Two ways in which this has been done are resonant small-angle soft X-ray scattering (RSoXS) [37,38] and scanning transmission X-ray microscopy (STXM) [39,40]. STXM provides direct, real-space morphological information on scales down to 30 nm and can be highly quantitative [41,42]. For analysis of RSoXS data and to choose the energies at which to take such data, it is necessary to have accurate reference XANES spectra of the components, which can be done with STXM [41].

The 5.3.2.2 low-energy ("Polymer") STXM at ALS [8] is ideally suited to these applications as it covers the CNO edges with sub-100meV energy resolution at the C edge. Fig. 5 shows an example (unpublished, provided by N. Holmes) of STXM morphology mapping. This was done by taking images at a number of energies to get XANES spectra at each pixel, then fitting these spectra to carefully-acquired reference spectra taken on uniform films. The components, TQ1 and PC71BM, are described in [43].

4.2. Organics and metals in the environment

The ability to study C speciation over many square microns of area with tens of nanometer resolution is useful in studying a number of systems drawn from the natural environment. Examples include aerosols in the atmosphere [44], associations of organics and Fe and Ca [45], and the preservation and transport of Fe-bearing particles from hydrothermal plumes in the ocean [46]. We will discuss the latter example in a bit more detail. The cycling of Fe in the ocean has important implications for the C cycle as Fe is a limiting nutrient for phytoplankton. Particulate Fe particles were filtered from ocean water at various depths and distances from hydrothermal vents along the East Pacific Rise at latitudes 9N (1st citation) and 15S (2nd). In both studies, Fe was found associated with organic detritus, but in the former, much

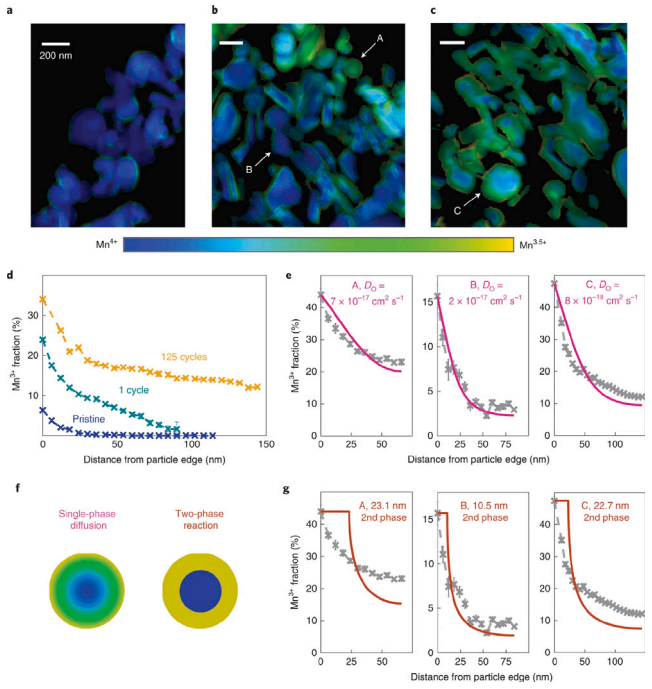

Fig. 6. Spectro-ptychography analysis of oxidations states of Mn in the cathode material $Li_{1.18-x}Ni_{0.21}Mn_{0.53}Co_{0.08}O_{2-\delta}$ measured for the pristine material (a), after 1 cycle (b) and after 125 cycles (c). A reduced state indicates oxygen vacancy and the profile of the density of vacancies from the particle surface to its center indicates a single phase diffusion process.
Source: Figure from [47].

of it was found to be in the soluble Fe(II) form, which might be expected to oxidize quickly and dissolve away. It was hypothesized that organic ligands bound the Fe(II), stabilizing it. In the latter study, organic-associated Fe(III) particles were found thousands of kilometers from the source, even though isolated Fe oxide particles would have sunk to the bottom. The low specific gravity of the organic matrix presumably kept the particles adrift.

4.3. Mapping oxygen vacancies in battery cathode primary particles

The ability to map transition metal oxidation states with nanometer spatial resolution over many micrometers of material has had a profound impact on the study of energy storage materials. The oxidation state of the transition metal cation can indicate a variety of phenomena but Csernica et al. [47] explore oxygen release in the layered oxide cathode material $Li_{1.18-x}Ni_{0.21}Mn_{0.53}Co_{0.08}O_{2-\delta}$. They utilize a novel ultramicrotomy technique to produce thin sections of the positive electrode, thereby maintaining the relationship of all secondary particles and allowing a visualization of heterogeneity across the entire electrode. Distributions across single primary particles, Fig. 6, about 200 nm across, are investigated with spectro-ptychography at the Mn L-edge. Mn reduction along the particle edges is observed after only a single cycle. With further cycling, this reduction extends into the particle interior with a profile that indicates that oxygen release is governed by chemical diffusion rather than a two phase reaction.

4.4. Operando electro-catalysis and analog memory devices

In this section we will present two examples of how *in-operando* capabilities at the ALS STXMs have contributed to our understanding of how chemical and electronic devices work under realistic conditions. In the first example Co based hydroxide electrocatalyst nanoparticles were investigated [48]. Laboratory based scanning microscopy studies of these materials show that the electrochemical current is mainly restricted to the edges of the nanoparticles. The question that can then be addressed using STXM is if this behavior is correlated with a non-homogeneous change of the chemical state during the electrochemical process. Fig. 7 summarizes the results of the STXM part of the study. The upper left panel in the figure shows the setup. The sample is confined to the electrochemical cell and in solution. The thickness of the solution is several hundreds of nm. Panel (b.) shows X-ray absorption spectra averaged over the entire particle while a voltage is applied and the particles are electrochmically active. The panel also shows reference spectra for Co^{2+},Co^{3+} and $Co^{3.6+}$. One finds that none of the observed Co spectra contain a significant fraction of Co with an oxidation state higher than 3+. This by itself is already important information since theoretical models exist that suggest that the final state of the reaction is Co4+. The second observation is that around 1.6 V the chemical maps become quite heterogeneous and one finds that Co sites at the edges of the particle tend to be less oxidized. This supports the finding of conventional scanning techniques that observed that the edges of the sample are the active sites for the so-called Oxygen Evolution Reaction.

The second example addresses an interesting issue in materials science. So called memristors are electronic components that couple electric charge to magnetic flux, similar in the way as a resistor couples current and voltage. However, in contrast a memristor is a highly non-linear device which makes it very appealing for complex computing applications like e.g. neuromorphic computing. In recent years it has become clear that the incorporation of a true memristor in an electrical circuit is too challenging. For this reason the research has been focusing instead on the design of *memristive devices*, which are devices that couple voltage with current in the same non linear manner as a true memristor couples charge and magnetic flux. Titanium dioxide and Vanadium dioxide have been suggested as potential materials. In order to fabricate and design reliable devices it is important to understand how they behave if a voltage is applied and in particular what happens at the oxygen sites in the material [49]. It is also crucial to understand how these devices might fail or change with temperature since the devices will heat up during operation. For this reason it is required to study how the electronic and potentially crystallographic structure changes with temperature [50]. Both of these questions have been addressed using ALS STXMs and we will briefly discuss the temperature dependent study here. Around 340K, VO_2 undergoes a metal to insulator transition as well as a structural transition from a rutile to a monoclinic phase. However, if one studies these transitions with different methods like e.g. optical or electrical transport, one finds that the observed transition temperatures depend on the methods, which has puzzled researchers for almost a century. In particular, optical transitions appear at lower temperature. Fig. 8 shows the results of the X-ray microscopy study that set out to find a microscopic origin for the macroscopic observed behavior. STXM images were obtained at two different photon energies that are typical for either structural changes (530 eV) or conductivity (528.7 eV). Both image series show that the transition from one phase to the other is not homogeneous, neither in the conductivity phase or in the structural phase. There is a large range of temperatures around 325 K where both phases co-exist. However, the effect of this heterogeneity on light transmission is different from its effect on conductivity. For metallic islands to contribute to macroscopic conductivity they need to be connected or at least exhibit a significant spatial density. On the other hand, each metallic island contributes equally to the optical properties of the device, which is why the optical curves are shifted to lower temperatures. This is another example of how a spectromicroscopic study of a material under operando conditions can give a clear answer to a scientific question by providing direct insight about the electronic structure on the nanoscale.

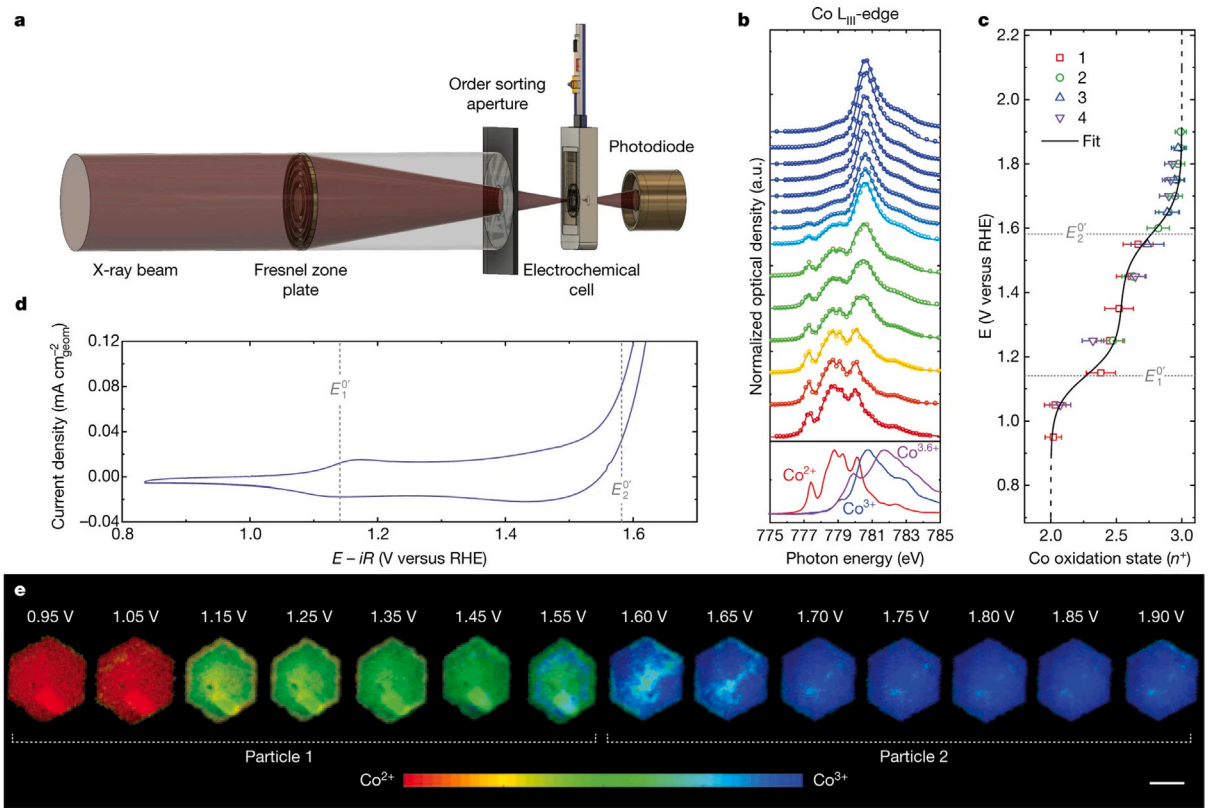

Fig. 7. (a) Experimental setup showing the electrochemical flow cell coupled into the STXM microscope. (b) Voltage-dependent particle-averaged Co LIII-edge STXM-XAS spectra. (c) Co oxidation state plotted with voltage, with an ideal solution model fit for four separate particles. (d) Cyclic voltammogram (in 0.1 M KOH) of β-Co(OH)2 in the STXM electrochemical flow cell at a scan rate of 10 mV s-1 and a flow rate of 30 μl min-1. (e) Steady-state voltage-dependent Co oxidation state phase maps of β-Co(OH)2 particles 1 and 2. Scale bar, 1 μm.
Source: Figure from [48].

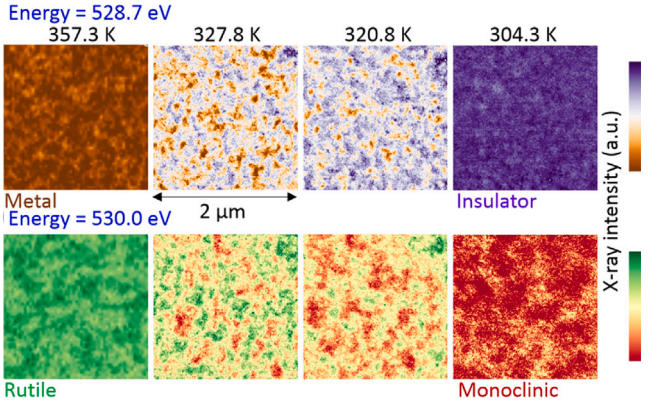

Fig. 8. Series of images taken at two different energies at the O K resonance. The upper row shows the transition of the sample from metal to insulator, while the lower row shows the transition from rutile to monoclinic lattice.
Source: Figure from [50].

5. Outlook

The spatial, temporal and chemical resolution of scanning X-ray microscopy is ultimately limited by the brightness (coherent photon flux) of the X-ray source. These imaging methods and the exciting new computational methods which naturally extend from them have been a primary justification for the upgrade of synchrotron sources around the world to provide diffraction limited X-ray beams. These new sources, of which an upgraded ALS storage ring is one such example (ALS-U), will be able to provide more than two orders of magnitude increased coherent photon flux over typical energy ranges [51]. In the soft X-ray range, where imaging at only a few times the wavelength has already been demonstrated, only modest gains in spatial resolution can be achieved from such large increases in coherent flux, though this would allow microscopes to approach imaging with a spatial resolution of down to a few nanometers [6]. Far more revolutionary gains will be had in the time domain as data will be generated more than 100 times faster than today. These gains will lead to scan-point dwell times of 1 microsecond for conventional imaging and 1 ms for ptychographic imaging. Such speeds could enable the acquisition of spectroscopic tomograms in hours rather than days but the high intensity will also exacerbate the existing problem of radiation damage, particularly with soft materials like polymers. The use of cryogenic sample environments should become much more routine. Significant development is needed to increase the speeds of commonly used scanning systems, to reach video frame rate scanning, and for soft X-ray pixel detectors which should reach frame rates of up to 10,000 frames per second or more to make use of the available coherent flux.

Declaration of competing interest

The authors declare the following financial interests/personal relationships which may be considered as potential competing interests: Thomas Feggeler reports financial support was provided by National Science Foundation. Thomas Feggeler reports financial support was provided by Lawrence Berkeley National Laboratory Lab Directed Research Development. Abraham Levitan reports financial support was

provided by Lawrence Berkeley National Laboratory Advanced Light Source. Abraham Levitan reports financial support was provided by US Department of Energy Office of Science - Science Graduate Student Research Fellowship. Hendrik Ohldag reports financial support was provided by Lawrence Berkeley National Laboratory Lab Directed Research Development.

Data availability

Data will be made available on request.

Acknowledgments

T.F. acknowledges support from STROBE: A National Science Foundation Science & Technology Center, United States, under Grant No. DMR-1548924. H.O. and T.F. acknowledge Lawrence Berkeley National Laboratory, United States for funding through LDRD Award: Development of a Continuous Photon Counting Scheme for Time Resolved Studies. A.L. acknowledges support in part by an ALS Doctoral Fellowship. This material is based upon work supported by the U.S. Department of Energy, Office of Science, Office of Workforce Development for Teachers and Scientists, Office of Science Graduate Student Research (SCGSR) program. The SCGSR program is administered by the Oak Ridge Institute for Science and Education (ORISE) for the DOE. ORISE is managed by ORAU under contract number DE-SC0014664. All opinions expressed in this paper are the author's and do not necessarily reflect the policies and views of DOE, ORAU, or ORISE. This research used resources of the Advanced Light Source, a U.S. DOE Office of Science User Facility under contract no. DE-AC02-05CH11231.

References

[1] J. Kirz, H. Ade, C. Jacobsen, C.-H. Ko, S. Lindaas, I. McNulty, D. Sayre, S. Williams, X. Zhang, M. Howells, Soft X-ray microscopy with coherent X rays (invited), Rev. Sci. Instrum. 63 (1) (1992) 557–563, http://dx.doi.org/10.1063/1.1142705.

[2] J. Kirz, H. Rarback, Soft X-ray microscopes, Rev. Sci. Instrum. 56 (1) (1985) 1–13, http://dx.doi.org/10.1063/1.1138464.

[3] W. Meyer-Ilse, M. Koike, H.R. Beguiristain, J.M. Maser, D.T.A. Jr., X-ray microscopy resource center at the advanced light source, in: C.J. Jacobsen, J.E. Trebes (Eds.), Soft X-ray Microscopy, vol. 1741, International Society for Optics and Photonics, SPIE, 1993, pp. 112–115, http://dx.doi.org/10.1117/12.138759.

[4] T. Warwick, K. Franck, J.B. Kortright, G. Meigs, M. Moronne, S. Myneni, E. Rotenberg, S. Seal, W.F. Steele, H. Ade, A. Garcia, S. Cerasari, J. Denlinger, S. Hayakawa, A.P. Hitchcock, T. Tyliszczak, J. Kikuma, E.G. Rightor, H.-J. Shin, B.P. Tonner, A scanning transmission X-ray microscope for materials science spectromicroscopy at the advanced light source, Rev. Sci. Instrum. 69 (8) (1998) 2964–2973, http://dx.doi.org/10.1063/1.1149041.

[5] A. Warwick, H.A. Padmore, H. Ade, Bend magnet beamline for scanning transmission X-ray microscopy at the Advanced Light Source, in: I. McNulty (Ed.), X-ray Microfocusing: Applications and Techniques, vol. 3449, International Society for Optics and Photonics, SPIE, 1998, pp. 12–18, http://dx.doi.org/10.1117/12.330337.

[6] D.A. Shapiro, S. Babin, R.S. Celestre, W. Chao, R.P. Conley, P. Denes, B. Enders, P. Enfedaque, S. James, J.M. Joseph, H. Krishnan, S. Marchesini, K. Muriki, K. Nowrouzi, S.R. Oh, H. Padmore, T. Warwick, L. Yang, V.V. Yashchuk, Y.-S. Yu, J. Zhao, An ultrahigh-resolution soft X-ray microscope for quantitative analysis of chemically heterogeneous nanomaterials, Sci. Adv. 6 (51) (2020) eabc4904, http://dx.doi.org/10.1126/sciadv.abc4904.

[7] H. Bluhm, K. Andersson, T. Araki, K. Benzerara, G. Brown, J. Dynes, S. Ghosal, M. Gilles, H.-C. Hansen, J. Hemminger, A. Hitchcock, G. Ketteler, A. Kilcoyne, E. Kneedler, J. Lawrence, G. Leppard, J. Majzlam, B. Mun, S. Myneni, A. Nilsson, H. Ogasawara, D. Ogletree, K. Pecher, M. Salmeron, D. Shuh, B. Tonner, T. Tyliszczak, T. Warwick, T. Yoon, Soft X-ray microscopy and spectroscopy at the molecular environmental science beamline at the Advanced Light Source, J. Electron Spectrosc. Relat. Phenom. 150 (2) (2006) 86–104, http://dx.doi.org/10.1016/j.elspec.2005.07.005, Science and Spectroscopy of Environmentally Important Interfaces.

[8] A.L.D. Kilcoyne, T. Tyliszczak, W.F. Steele, S. Fakra, P. Hitchcock, K. Franck, E. Anderson, B. Harteneck, E.G. Rightor, G.E. Mitchell, A.P. Hitchcock, L. Yang, T. Warwick, H. Ade, Interferometer-controlled scanning transmission X-ray microscopes at the Advanced Light Source, J. Synchrotron Radiat. 10 (2) (2003) 125–136, http://dx.doi.org/10.1107/s0909049502017739.

[9] D. Shapiro, S. Roy, R. Celestre, W. Chao, D. Doering, M. Howells, S. Kevan, D. Kilcoyne, J. Kirz, S. Marchesini, K.A. Seu, A. Schirotzek, J. Spence, T. Tyliszczak, T. Warwick, D. Voronov, H.A. Padmore, Development of coherent scattering and diffractive imaging and the COSMIC facility at the Advanced Light Source, J. Phys. Conf. Ser. 425 (19) (2013) 192011, http://dx.doi.org/10.1088/1742-6596/425/19/192011.

[10] R. Celestre, K. Nowrouzi, D.A. Shapiro, P. Denes, J.M. Joseph, A. Schmid, H.A. Padmore, Nanosurveyor 2: A compact instrument for nano-tomography at the advanced light source, J. Phys. Conf. Ser. 849 (1) (2017) 012047, http://dx.doi.org/10.1088/1742-6596/849/1/012047.

[11] T. Tyliszczak, T. Warwick, A.L.D. Kilcoyne, S. Fakra, D.K. Shuh, T.H. Yoon, J. Brown, S. Andrews, V. Chembrolu, J. Strachan, Y. Acremann, Soft X-ray scanning transmission microscope working in an extended energy range at the advanced light source, AIP Conf. Proc. 705 (1) (2004) 1356–1359, http://dx.doi.org/10.1063/1.1758053.

[12] A.P. Hitchcock, Z. Qin, S.M. Rosendahl, V. Lee, M. Reynolds, H. Hosseinkhannazer, Electro-deposition of Cu studied with in situ electrochemical scanning transmission X-ray microscopy, AIP Conf. Proc. 1696 (1) (2016) http://dx.doi.org/10.1063/1.4937497.

[13] P. Thibault, M. Dierolf, A. Menzel, O. Bunk, C. David, F. Pfeiffer, High-resolution scanning X-ray diffraction microscopy, Science 321 (2008) 379–382, http://dx.doi.org/10.1126/science.1158573.

[14] D.A. Shapiro, Y.-S. Yu, T. Tyliszczak, J. Cabana, R. Celestre, W. Chao, K. Kaznatcheev, A.L.D. Kilcoyne, F. Maia, S. Marchesini, Y.S. Meng, T. Warwick, L.L. Yang, H.A. Padmore, Chemical composition mapping with nanometre resolution by soft X-ray microscopy, Nat. Photonics 8 (10) (2014) 765–769, http://dx.doi.org/10.1038/nphoton.2014.207.

[15] M.A. Marcus, D.A. Shapiro, Y.-S. Yu, Ptychography reduces spectral distortions intrinsic to conventional zone-plate-based X-ray spectromicroscopy, Microsc. Microanal. 27 (6) (2021) 1448–1453, http://dx.doi.org/10.1017/S1431927621012733.

[16] M.A. Marcus, Data analysis in spectroscopic STXM, J. Electron Spectrosc. Relat. Phenom. 264 (2023) 147310, http://dx.doi.org/10.1016/j.elspec.2023.147310.

[17] J.-D. Förster, C. Gurk, M. Lamneck, H. Tong, F. Ditas, S.S. Steimer, P.A. Alpert, M. Ammann, J. Raabe, M. Weigand, B. Watts, U. Pöschl, M.O. Andreae, C. Pöhlker, MIMiX: a Multipurpose In situ Microreactor system for X-ray microspectroscopy to mimic atmospheric aerosol processing, Atmos. Meas. Tech. 13 (7) (2020) 3717–3729, http://dx.doi.org/10.5194/amt-13-3717-2020.

[18] W.E. Bailey, L. Cheng, D.J. Keavney, C.-C. Kao, E. Vescovo, D.A. Arena, Precessional dynamics of elemental moments in a ferromagnetic alloy, Phys. Rev. B 70 (2004) 172403, http://dx.doi.org/10.1103/PhysRevB.70.172403.

[19] G. Boero, S. Rusponi, P. Bencok, R.S. Popovic, H. Brune, P. Gambardella, X-ray ferromagnetic resonance spectroscopy, Appl. Phys. Lett. 87 (15) (2005) 152503, http://dx.doi.org/10.1063/1.2089180.

[20] J. Goulon, A. Rogalev, F. Wilhelm, N. Jaouen, C. Goulon-Ginet, G. Goujon, J. Ben Youssef, M.V. Indenbom, X-ray detected magnetic resonance at the fe K-edge in YIG: Forced precession of magnetically polarized orbital components, J. Exp. Theor. Phys. Lett. 82 (11) (2005) 696–701, http://dx.doi.org/10.1134/1.2171722.

[21] G. Boero, S. Rusponi, J. Kavich, A.L. Rizzini, C. Piamonteze, F. Nolting, C. Tieg, J.-U. Thiele, P. Gambardella, Longitudinal detection of ferromagnetic resonance using X-ray transmission measurements, Rev. Sci. Instrum. 80 (12) (2009) 123902, http://dx.doi.org/10.1063/1.3267192.

[22] M.K. Marcham, P.S. Keatley, A. Neudert, R.J. Hicken, S.A. Cavill, L.R. Shelford, G. van der Laan, N.D. Telling, J.R. Childress, J.A. Katine, P. Shafer, E. Arenholz, Phase-resolved X-ray ferromagnetic resonance measurements in fluorescence yield, J. Appl. Phys. 109 (7) (2011) 07D353, http://dx.doi.org/10.1063/1.3567143.

[23] W.E. Bailey, C. Cheng, R. Knut, O. Karis, S. Auffret, S. Zohar, D. Keavney, P. Warnicke, J.-S. Lee, D.A. Arena, Detection of microwave phase variation in nanometre-scale magnetic heterostructures, Nature Commun. 4 (1) (2013) 2025, http://dx.doi.org/10.1038/ncomms3025.

[24] K. Ollefs, R. Meckenstock, D. Spoddig, F.M. Römer, C. Hassel, C. Schöppner, V. Ney, M. Farle, A. Ney, Toward broad-band X-ray detected ferromagnetic resonance in longitudinal geometry, J. Appl. Phys. 117 (22) (2015) 223906, http://dx.doi.org/10.1063/1.4922248.

[25] M. Weigand, S. Wintz, J. Gräfe, M. Noske, H. Stoll, B. Van Waeyenberge, G. Schütz, TimeMaxyne: A shot-noise limited, time-resolved pump-and-probe acquisition system capable of 50 GHz frequencies for synchrotron-based X-ray microscopy, Crystals 12 (8) (2022) http://dx.doi.org/10.3390/cryst12081029.

[26] T. Feggeler, R. Meckenstock, D. Spoddig, B.W. Zingsem, H. Ohldag, H. Wende, M. Farle, M. Winklhofer, K.J. Ollefs, Spatially resolved ghz magnetization dynamics of a magnetite nano-particle chain inside a magnetotactic bacterium, Phys. Rev. Res. 3 (2021) 033036, http://dx.doi.org/10.1103/PhysRevResearch.3.033036.

[27] N. Träger, F. Lisiecki, R. Lawitzki, M. Weigand, H. Głowiński, G. Schütz, G. Schmitz, P. Kuświk, M. Krawczyk, J. Gräfe, P. Gruszecki, Competing spin wave emission mechanisms revealed by time-resolved X-ray microscopy, Phys. Rev. B 103 (2021) 014430, http://dx.doi.org/10.1103/PhysRevB.103.014430.

[28] S. Bonetti, R. Kukreja, Z. Chen, D. Spoddig, K. Ollefs, C. Schöppner, R. Meckenstock, A. Ney, J. Pinto, R. Houanche, J. Frisch, J. Stöhr, H.A. Dürr, H. Ohldag, Microwave soft X-ray microscopy for nanoscale magnetization dynamics in the 5–10 GHz frequency range, Rev. Sci. Instrum. 86 (9) (2015) 093703, http://dx.doi.org/10.1063/1.4930007.

[29] A. Puzic, B. Van Waeyenberge, K.W. Chou, P. Fischer, H. Stoll, G. Schütz, T. Tyliszczak, K. Rott, H. Brückl, G. Reiss, I. Neudecker, T. Haug, M. Buess, C.H. Back, Spatially resolved ferromagnetic resonance: Imaging of ferromagnetic eigenmodes, J. Appl. Phys. 97 (10) (2005) 10E704, http://dx.doi.org/10.1063/1.1860971.

[30] R. Narkowicz, D. Suter, R. Stonies, Planar microresonators for EPR experiments, J. Magn. Reson. 175 (2) (2005) 275–284, http://dx.doi.org/10.1016/j.jmr.2005.04.014.

[31] B. Zingsem, T. Feggeler, R. Meckenstock, D. Spoddig, T. Schaffers, S. Pile, H. Ohldag, M. Farle, H. Wende, A. Ney, K. Ollefs, Evaluation protocol for revealing magnonic contrast in TR-STXM measurements, AIP Adv. 13 (4) (2023) http://dx.doi.org/10.1063/5.0145753.

[32] E. Albisetti, S. Tacchi, R. Silvani, G. Scaramuzzi, S. Finizio, S. Wintz, C. Rinaldi, M. Cantoni, J. Raabe, G. Carlotti, R. Bertacco, E. Riedo, D. Petti, Optically inspired nanomagnonics with nonreciprocal spin waves in synthetic antiferromagnets, Adv. Mater. 32 (9) (2020) 1906439, http://dx.doi.org/10.1002/adma.201906439.

[33] E. Albisetti, D. Petti, G. Sala, R. Silvani, S. Tacchi, S. Finizio, S. Wintz, A. Calò, X. Zheng, J. Raabe, E. Riedo, R. Bertacco, Nanoscale spin-wave circuits based on engineered reconfigurable spin-textures, Commun. Phys. 1 (1) (2018) 56, http://dx.doi.org/10.1038/s42005-018-0056-x.

[34] A.L. Levitan, K. Keskinbora, U.T. Sanli, M. Weigand, R. Comin, Single-frame far-field diffractive imaging with randomized illumination, Opt. Express 28 (25) (2020) 37103, http://dx.doi.org/10.1364/OE.397421.

[35] A. Levitan, Studying Electronic Textures with Coherent Lensless Imaging (Ph.D. thesis), Massachusetts Instute of Technology, Cambridge, MA, USA, 2023.

[36] Y. Li, W. Huang, D. Zhao, L. Wang, Z. Jiao, Q. Huang, P. Wang, M. Sun, G. Yuan, Recent progress in organic solar cells: A review on materials from acceptor to donor, Molecules 27 (6) (2022) http://dx.doi.org/10.3390/molecules27061800.

[37] T.P. Chaney, A.J. Levin, S.A. Schneider, M.F. Toney, Scattering techniques for mixed donor–acceptor characterization in organic photovoltaics, Mater. Horiz. 9 (2022) 43–60, http://dx.doi.org/10.1039/D1MH01219C.

[38] B.A. Collins, E. Gann, Resonant soft X-ray scattering in polymer science, J. Polym. Sci. 60 (7) (2022) 1199–1243, http://dx.doi.org/10.1002/pol.20210414.

[39] O. Alqahtani, M. Babics, J. Gorenflot, V. Savikhin, T. Ferron, A.H. Balawi, A. Paulke, Z. Kan, M. Pope, A.J. Clulow, J. Wolf, P.L. Burn, I.R. Gentle, D. Neher, M.F. Toney, F. Laquai, P.M. Beaujuge, B.A. Collins, Mixed domains enhance charge generation and extraction in bulk-heterojunction solar cells with small-molecule donors, Adv. Energy Mater. 8 (19) (2018) 1702941, http://dx.doi.org/10.1002/aenm.201702941.

[40] I. Persson, H. Laval, S. Chambon, G. Bonfante, K. Hirakawa, G. Wantz, B. Watts, M.A. Marcus, X. Xu, L. Ying, G. Lakhwani, M.R. Andersson, J.M. Cairney, N.P. Holmes, Sub-4 nm mapping of donor–acceptor organic semiconductor nanoparticle composition, Nanoscale 15 (2023) 6126–6142, http://dx.doi.org/10.1039/D3NR00839H.

[41] B.A. Collins, H. Ade, Quantitative compositional analysis of organic thin films using transmission NEXAFS spectroscopy in an X-ray microscope, J. Electron Spectrosc. Relat. Phenom. 185 (5) (2012) 119–128, http://dx.doi.org/10.1016/j.elspec.2012.05.002.

[42] B.A. Collins, Z. Li, J.R. Tumbleston, E. Gann, C.R. McNeill, H. Ade, Absolute measurement of domain composition and nanoscale size distribution explains performance in PTB7:PC71BM solar cells, Adv. Energy Mater. 3 (1) (2013) 65–74, http://dx.doi.org/10.1002/aenm.201200377.

[43] N.P. Holmes, M. Marks, P. Kumar, R. Kroon, M.G. Barr, N. Nicolaidis, K. Feron, A. Pivrikas, A. Fahy, A.D. de Zerio Mendaza, A. Kilcoyne, C. Müller, X. Zhou, M.R. Andersson, P.C. Dastoor, W.J. Belcher, Nano-pathways: Bridging the divide between water-processable nanoparticulate and bulk heterojunction organic photovoltaics, Nano Energy 19 (2016) 495–510, http://dx.doi.org/10.1016/j.nanoen.2015.11.021.

[44] N.N. Lata, Z. Cheng, D. Dexheimer, D. Zhang, F. Mei, S. China, Vertical gradient of size-resolved aerosol compositions over the arctic reveals cloud processed aerosol in-cloud and above cloud, Environ. Sci. Technol. 57 (14) (2023) 5821–5830, http://dx.doi.org/10.1021/acs.est.2c09498.

[45] P.S.P. Arachchige, G.M. Hettiarachchi, C.W. Rice, J.J. Dynes, L. Maurmann, J. Wang, C. Karunakaran, A.L.D. Kilcoyne, C.P. Attanayake, T.J.C. Amado, J.E. Fiorin, Sub-micron level investigation reveals the inaccessibility of stabilized carbon in soil microaggregates, Sci. Rep. 8 (1) (2018) 16810, http://dx.doi.org/10.1038/s41598-018-34981-9.

[46] B.M. Toner, S.C. Fakra, S.J. Manganini, C.M. Santelli, M.A. Marcus, J.W. Moffett, O. Rouxel, C.R. German, K.J. Edwards, Preservation of iron(II) by carbon-rich matrices in a hydrothermal plume, Nat. Geosci. 2 (3) (2009) 197–201, http://dx.doi.org/10.1038/ngeo433.

[47] P.M. Csernica, S.S. Kalirai, W.E. Gent, K. Lim, Y.-S. Yu, Y. Liu, S.-J. Ahn, E. Kaeli, X. Xu, K.H. Stone, A.F. Marshall, R. Sinclair, D.A. Shapiro, M.F. Toney, W.C. Chueh, Persistent and partially mobile oxygen vacancies in Li-rich layered oxides, Nat. Energy 6 (6) (2021) 642–652, http://dx.doi.org/10.1038/s41560-021-00832-7, Number: 6 Publisher: Nature Publishing Group.

[48] J.T. Mefford, A.R. Akbashev, M. Kang, C.L. Bentley, W.E. Gent, H.D. Deng, D.H. Alsem, Y.-S. Yu, N.J. Salmon, D.A. Shapiro, P.R. Unwin, W.C. Chueh, Correlative operando microscopy of oxygen evolution electrocatalysts, Nature 593 (7857) (2021) 67–73, http://dx.doi.org/10.1038/s41586-021-03454-x.

[49] S. Kumar, C.E. Graves, J.P. Strachan, E.M. Grafals, A.L.D. Kilcoyne, T. Tyliszczak, J.N. Weker, Y. Nishi, R.S. Williams, Direct observation of localized radial oxygen migration in functioning tantalum oxide memristors, Adv. Mater. 28 (14) (2016) 2772–2776, http://dx.doi.org/10.1002/adma.201505435.

[50] S. Kumar, J.P. Strachan, A.L.D. Kilcoyne, T. Tyliszczak, M.D. Pickett, C. Santori, G. Gibson, R.S. Williams, The phase transition in VO2 probed using X-ray, visible and infrared radiations, Appl. Phys. Lett. 108 (7) (2016) http://dx.doi.org/10.1063/1.4939746.

[51] A. White, K. Goldberg, S. Kevan, D. Leitner, D. Robin, C. Steier, L. Yarris, A new light for berkeley lab—the advanced light source upgrade, Synchrotron Radiat. News 32 (1) (2019) 32–36, http://dx.doi.org/10.1080/08940886.2019.1559608.